JOURNAL OF THE ROYAL SOCIETY Interface

J. R. Soc. Interface (2010) **7**, 1665–1676
doi:10.1098/rsif.2010.0281
Published online 21 July 2010

High-resolution tomographic imaging of a human cerebellum: comparison of absorption and grating-based phase contrast

Georg Schulz[1,*], Timm Weitkamp[2], Irene Zanette[2], Franz Pfeiffer[3], Felix Beckmann[4], Christian David[5], Simon Rutishauser[5], Elena Reznikova[6] and Bert Müller[1]

[1]*Biomaterials Science Center, University of Basel, Basel, Switzerland*
[2]*European Synchrotron Radiation Facility, Grenoble, France*
[3]*Department of Physics/Biophysics (E17), Technische Universität München, Garching, Germany*
[4]*Institute for Materials Research, GKSS Research Centre, Geesthacht, Germany*
[5]*Laboratory for Micro- and Nanotechnology, Paul Scherrer Institut, Villigen, Switzerland*
[6]*Institute of Microstructure Technology, Karlsruhe Institute for Technology, Karlsruhe, Germany*

Human brain tissue belongs to the most impressive and delicate three-dimensional structures in nature. Its outstanding functional importance in the organism implies a strong need for brain imaging modalities. Although magnetic resonance imaging provides deep insights, its spatial resolution is insufficient to study the structure on the level of individual cells. Therefore, our knowledge of brain microstructure currently relies on two-dimensional techniques, optical and electron microscopy, which generally require severe preparation procedures including sectioning and staining. X-ray absorption microtomography yields the necessary spatial resolution, but since the composition of the different types of brain tissue is similar, the images show only marginal contrast. An alternative to absorption could be X-ray phase contrast, which is known for much better discrimination of soft tissues but requires more intricate machinery. In the present communication, we report an evaluation of the recently developed X-ray grating interferometry technique, applied to obtain phase-contrast as well as absorption-contrast synchrotron radiation-based microtomography of human cerebellum. The results are quantitatively compared with synchrotron radiation-based microtomography in optimized absorption-contrast mode. It is demonstrated that grating interferometry allows identifying besides the blood vessels, the stratum moleculare, the stratum granulosum and the white matter. Along the periphery of the stratum granulosum, we have detected microstructures about 40 μm in diameter, which we associate with the Purkinje cells because of their location, size, shape and density. The detection of individual Purkinje cells without the application of any stain or contrast agent is unique in the field of computed tomography and sets new standards in non-destructive three-dimensional imaging.

Keywords: synchrotron radiation-based microtomography; absorption contrast; X-ray phase contrast; X-ray grating interferometry; X-ray Talbot interferometry; human brain tissue

1. INTRODUCTION

With more than 50 billion neurons, most of them located in the cerebellar cortex, the human cerebellum includes around 50 per cent of the neurons of the entire brain (Trepel 2008). *Purkinje* cells are the largest cells of the cerebellum exhibiting spherical shapes with diameters of about 40–70 μm. These cells form the nerve centre where the impulses of almost all neurons of the cerebellar cortex converge and are transferred to their destination beyond the cortex. Today, only two-dimensional methods, such as conventional histology and fluorescence microscopy, serve for Purkinje cell visualization. They include serious preparation steps, namely sectioning and staining. Sectioning destroys the three-dimensional nature of the brain specimens and the subsequent preparation steps induce local shrinkage, which requires correction of

*Author for correspondence (georg.schulz@unibas.ch).

Received 25 May 2010
Accepted 29 June 2010

This journal is © 2010 The Royal Society

the images (Germann *et al.* 2008). Therefore, non-destructive three-dimensional imaging techniques should be identified that provide enough contrast between internal features of the human cerebellum and also offer sufficient spatial resolution for uncovering individual cells—if possible, without selective staining.

Magnetic resonance tomography (MRT) is well established for imaging human brain tissue. It yields superb contrast between white and grey matter, but only limited spatial resolution. At present, the best medical MRT scanners produce voxel lengths at least one order of magnitude larger than the typical diameter of Purkinje cells. Although clinical X-ray computed tomography (CT) can give better spatial resolution it also does not reach the level of individual cells. Osmium-stained, individual ganglion cells encircled by soft tissue of the human inner ear, however, have been made visible by synchrotron radiation-based microcomputed tomography (SRμCT), recently (Lareida *et al.* 2009). Together with the calculations on absorption contrast between white and grey matter (Brooks *et al.* 1980), we hypothesize that SRμCT with the advantages of high monochromatic photon flux and spatial coherence could generate detailed images of human cerebellum that give deep insight into the anatomy at the cellular level.

Nonetheless, considerable doubt remains as to whether the density resolution in absorption contrast mode will actually result in high-quality images of unstained brain tissue. Consequently, the phase-contrast mode should be evaluated as well. X-ray phase-contrast approaches apply a variety of different principles but are all based on the phase shifts of X-ray waves penetrating the specimen (Fitzgerald 2000; Momose 2005). Set-ups based on a *crystal interferometer* (Bonse & Hart 1965) provide a direct measure of the profile of phase shifts induced into the X-ray wave by the specimen. Such instrumentation was successfully applied to mouse kidney (Beckmann *et al.* 1995) and rat cerebellum (Momose & Fukuda 1995). The obtained data clearly visualize subtle differences in tissue density. Unfortunately, the field of view is limited as the result of technological constraints in building the crystal interferometer. Moreover, it is a fact that the requirements for the experimental conditions are more restrictive. The second, and probably most widely used, class of X-ray phase-contrast techniques is *propagation-based* or *inline* methods. They emerged in the mid-1990s, after the first third-generation synchrotron light sources went into operation (Snigirev *et al.* 1995; Cloetens *et al.* 1996). *Inline* phase contrast does not need additional optical components as the *Fresnel* diffraction in the space between the sample and detector creates the contrast. This approach works only reasonably well for the third-generation synchrotron light sources, which possess a sufficient degree of spatial coherence. One particularly successful implementation of quantitative *inline* phase contrast is a technique known as *holotomography*, in which images recorded at several distances behind the specimen are combined to quantitatively retrieve the phase shift (Cloetens *et al.* 1999). A prominent, recent example is the imaging of a fossilized fish (Pradel *et al.* 2009), containing the only known three-dimensional representation of a fossilized brain so far. The third approach, particularly relevant for soft tissues, is *analyser-based* imaging (ABI). Here, an analyser crystal is incorporated between the specimen and the detection unit to uncover the specimen-induced phase shift of the monochromatic X-rays (Förster *et al.* 1980; Davis *et al.* 1995). Combined with suitable data analysis, as shown for the *diffraction-enhanced imaging* (DEI) (Chapman *et al.* 1997), ABI gives access to absorption, refraction and scattering. Nevertheless, ABI requires a monochromatic X-ray beam with small divergence and high-quality, sufficiently large analyser crystals.

The recently developed *grating* or *Talbot* interferometry (David *et al.* 2002; Momose *et al.* 2003; Weitkamp *et al.* 2005; Pfeiffer *et al.* 2007*c*) is another, powerful phase-contrast technique. The X-ray interferometer consists of two line-grid structures placed between the specimen and the detector. Experiments on extracted rabbit liver (Momose *et al.* 2006), rat heart (Weitkamp *et al.* 2008) and rat brain (Pfeiffer *et al.* 2007*a*, 2009) have been performed. It has to be demonstrated, however, whether the spatial resolution of grating interferometry allows visualization of human brain tissue down to the level of individual cells.

The present communication aims at evaluating the potential of SRμCT in absorption and phase-contrast mode to reveal morphological features in human cerebellum, especially the white and grey matter as well as Purkinje cells.

2. MATERIAL AND METHODS

2.1. Preparation of the brain specimen

The specimen was extracted from the donated body of a 68 year old male. All procedures were conducted in accordance with the Declaration of Helsinki and according to the ethical guidelines of the Canton of Basel. The brain was extracted at the Institute of Anatomy (University of Basel, Switzerland) within 48 h after death, and subsequently transferred to 10 per cent formalin for fixation. After approximately three months of fixation, a small block of the cerebellum was extracted at the University Hospital Zurich, Switzerland. The size of the block is about $6 \times 6 \times 11\ \mathrm{mm}^3$. For the measurement, the block was placed and fixed in a 0.5 ml Eppendorf container filled with 4 per cent formalin solution.

2.2. Grating interferometry

The three-dimensional distribution of the complex refractive index of an object for X-rays of a given wavelength and photon energy can be written as

$$n(x,y,z) = 1 - \delta(x,y,z) + \mathrm{i}\beta(x,y,z). \tag{2.1}$$

The imaginary part $\beta(x,y,z)$ describes the absorption of X-rays in the sample. It is related to the widely used linear X-ray attenuation coefficient $\mu(x,y,z)$ by

$$\mu(x,y,z) = \frac{4\pi}{\lambda} \cdot \beta(x,y,z), \tag{2.2}$$

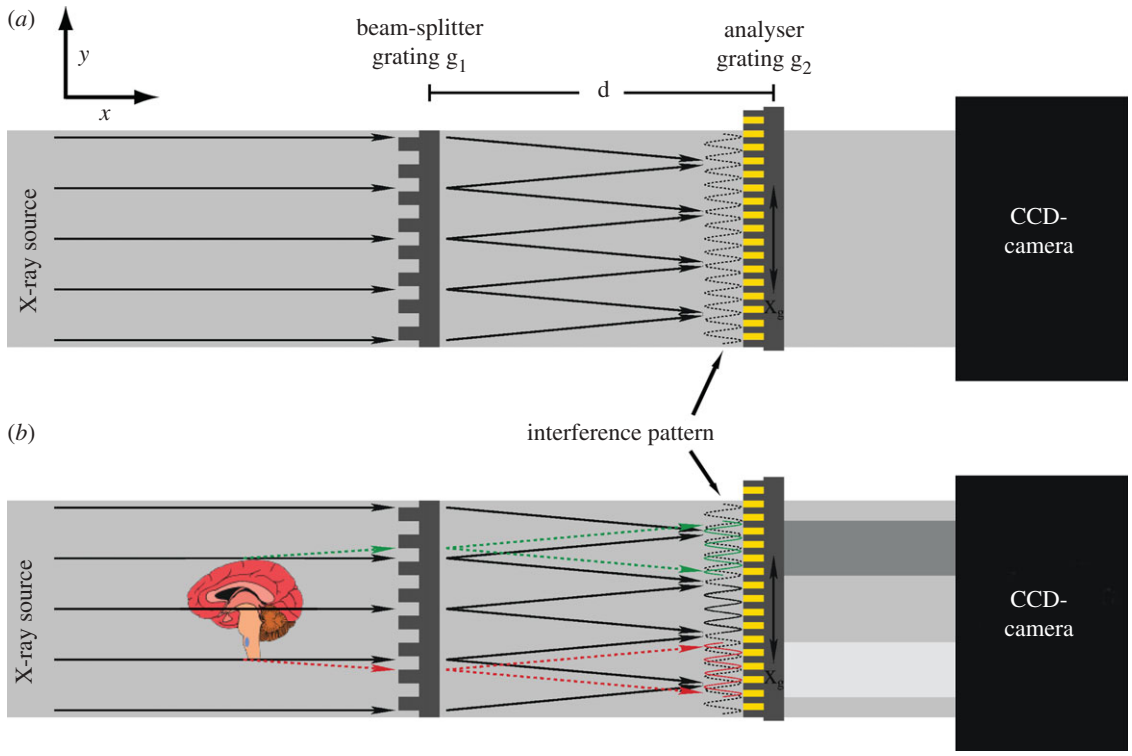

Figure 1. Top view of the experimental set-up consisting of the detector and the grating interferometer composed of a beam-splitter and an analyser grating. The x- and y-axis form a horizontal plane in which the coordinate x corresponds to the beam direction. The z-axis is oriented parallel to the x–y-plane in the direction of the viewer. The tomography rotation axis is oriented parallel to the z-axis. A phase object causes slight deflection of the incoming X-rays.

where λ is the wavelength of the incident X-rays. Conventional absorption tomography yields virtual slices or volume data corresponding to the local X-ray absorption coefficient $\mu(x,y,z)$.

Phase-contrast CT, on the other hand, provides the real part of the refractive index, often expressed in terms of its decrement from unity $\delta(x,y,z)$. It is related to the electron density distribution $\rho_e(x,y,z)$ by

$$\delta(x,y,z) = \frac{r_e \lambda^2}{2\pi} \rho_e(x,y,z), \tag{2.3}$$

for X-ray energies far away from the absorption edges. Here, the constant r_e is the classical electron radius.

For the detection of $\delta(x,y,z)$ a grating interferometer as schematically illustrated in figure 1 was used. Two gratings are arranged perpendicular to the incident X-ray beam. The *beam-splitter* grating g_1 consists of silicon stripes with the periodicity p_1 and a phase shift of $\Delta\varphi = \pi$ in the X-ray wave. The requirements of the grating thickness D and absorption contrast C are determined by equation (2.4) using spectral data of the real part of the refractive index decrement $\delta(\lambda)$ and the linear X-ray absorption coefficients $\mu(\lambda)$ for the grating materials.

$$\Delta\phi = 2\pi \frac{D \cdot \delta(\lambda)}{\lambda}; \quad C = \frac{1 - \exp(-\mu(\lambda) \cdot D)}{1 + \exp(-\mu(\lambda) \cdot D)}. \tag{2.4}$$

At the X-ray photon energy of 23 keV used, a Si grating g_1 with $D = 28.4\ \mu$m provides π phase shift and negligible absorption contrast of $C_{g_1} = 1.1 \times 10^{-2}$. The grating lines induce fringe patterns in the X-ray intensity distribution downstream. At distances from the beam-splitter grating of

$$d_n = \frac{n p_1^2}{8\lambda}, \tag{2.5}$$

the intensity fringe contrast takes extreme values, with maximal contrast for odd *Talbot* orders $n = 1, 3, 5, \ldots$, and vanishing contrast for even values of n (Weitkamp *et al.* 2006). The grating g_2, termed *analyser* grating, with a periodicity $p_2 \approx p_1/2$, should have strongly absorbing stripes with a contrast of $C_{g_2} \approx 1$, here made of gold. The absorption requirement to the X-ray analyser grating is important to obtain the maximum visibility of the moiré fringes and to demonstrate the extreme resolution of $\Delta\delta = 10^{-8}$–10^{-9} of the real part of the refractive index decrement for this X-ray Talbot interferometry phase-contrast CT imaging of fine structures of the brain specimen. The distance from grating g_1 to grating g_2 equals the *Talbot* distance d_n with an odd *Talbot* order n.

The beam-splitter grating g_1 was fabricated at the Paul Scherrer Institut (Villigen, Switzerland) in a process involving lithography and anisotropic wet-etching into <110>-oriented silicon (David *et al.* 2007). The analyser grating g_2 was fabricated at the Karlsruhe Institute of Technology (Karlsruhe, Germany) by soft X-ray lithography of SU-8 resist (Reznikova *et al.* 2008). The unique planar technology provides aspect ratios of more than 50 for SU-8 polymer lamellar submicron grating matrixes that are filled uniformly with electroplated gold. The SU-8 polymer

created during the X-ray exposure and post-exposure-bake processes has unequalled mechanical, chemical and radiation stability.

A phase object between the X-ray source and the grating interferometer disturbs the interference pattern by deflecting the X-rays (figure 1*b*). These deflections cause slight spatial shifts of the stripes in the pattern. The distortions cannot be detected directly, as the detector pixel size is larger than the displacements. Grating g_2 has the function of detecting the displacements by using a *phase-stepping* method. As additional information, the phase-stepping method also provides the relative attenuation factor besides the relative object's phase shift. A detailed description of grating interferometry and of the phase-stepping method is given in Weitkamp *et al.* (2005). The quantitative relation between local beam propagation direction $\alpha(y,z)$, wave phase shift $\Phi(y,z)$ and decrement of X-ray refractive index $\delta(x,y,z)$ is

$$\alpha(y,z) = \frac{\lambda}{2\pi}\frac{\partial \Phi(y,z)}{\partial y} = \int_{-\infty}^{\infty} \frac{\partial \delta(x,y,z)}{\partial y}\,\mathrm{d}x. \qquad (2.6)$$

Analysis of the phase-stepping data from the interferometer yields $\alpha(y,z)$. The projection of δ along the beam propagation direction can then be obtained by calculating the indefinite integral (or, in terms of discrete values, the cumulative sum) of α along y. Tomographic reconstruction then yields the three-dimensional distribution of δ. If the filtered backprojection method is used for the tomographic reconstruction, the integration of α can be included in the filter kernel (Pfeiffer *et al.* 2007*c*). This is different from most implementations of analyser crystal-based tomography, first demonstrated by Dilmanian *et al.* (2000), in which the tomographically reconstructed phase-related quantity is usually the gradient $\partial\delta/\partial z$, owing to the fact that both the tomography rotation axis and the diffraction plane are usually vertical, although occasional exceptions are reported (Maksimenko *et al.* 2005).

The influence of small angle scattering on the $\delta(x,y,z)$ distribution was neglected. This was justified because the scattering by the analysed specimen (human brain tissue) is very weak. In addition, while scattering affects the signal-to-noise ratio, it has no influence on the retrieved value of δ.

The grating interferometry experiments were performed at the beamline ID19 (ESRF, Grenoble, France; Weitkamp *et al.* 2010). X-rays were taken from a U32 undulator with its gap set to 15.15 mm. The photon energy of 23 keV was selected using a double-crystal Si(111) monochromator in Bragg geometry. During the experiment, the photon flux density at the beamline ID19 corresponded to 10^{11} photons $\mathrm{mm}^{-2}\,\mathrm{s}^{-1}$. With a resulting field of view of 10.4 mm width and 6.1 mm height, two scans at different height position of the specimen were acquired in order to image the entire cerebellum piece. The interferometer consisted of a beam-splitter grating g_1 with a periodicity of $p_1 = 4.785$ μm and a Si structure height of 29 μm, and an analyser grating g_2 with a periodicity of $p_2 = 2.400$ μm and a structure height of 50 μm corresponding to an absorption contrast value of $C_{g_2} = 0.993$. With a distance between source and interferometer of 150 m and a distance between the gratings of $d = 479.4$ mm (9th Talbot order), the ratio of the grating periods, p_2/p_1, was matched to the beam divergence (Weitkamp *et al.* 2006). The width of the contrast curve of a phase-stepping scan in this configuration was $p_2/(2d) = 2.5$ μrad (full width half maximum (FWHM)). This is comparable to the rocking curve width of a Si-333 analyser crystal at the same energy (2.4 μrad FWHM), which could thus be expected to yield images of similar angular sensitivity in an analyser-based imaging set-up. However, since the energy bandwidth of Si-333 at 23 keV is more than 15 times narrower than that of Si-111, such an ABI set-up would be substantially less photon efficient than the grating-based set-up used here.

The Eppendorf container with the cerebellum in formalin solution was fixed at the high precision rotation stage and immersed in a water tank with parallel polymethylmethacrylat plates for the measurements. Note that the water-filled tank is fixed during the whole experiment. For this reason, all the changes in the projections during the scan should have been cancelled by the flat-field projections. In addition, no visible changes on the polymer were seen after multiple days of measurements. This arrangement ensured minimized artefacts owing to X-ray phase curvature induced by the container surface. Specimen and tank were located about 10 cm upstream of the beam-splitter grating. The detector, placed about 3 cm downstream of the analyser grating, was a lens-coupled scintillator and charge-coupled device (CCD) system using a FReLoN 2K (Fast-Readout, Low-Noise, ESRF Grenoble, France) CCD with 2048×2048 pixels. The effective pixel size corresponded to 5.1 μm. Projection radiographs were taken in 1501 steps over a range of 360° (i.e. step size 0.24°). At each projection angle, four phase-stepping images were taken over one period of the interferometer fringe pattern. The exposure time for each image was 1 s.

Repeated measurements on the formalin fixated soft tissue showed reproducibility. No influence of X-rays on the specimen was detected.

2.3. SRμCT in absorption-contrast mode

SRμCT experiments in absorption-contrast mode were carried out at the beamline BW2 operated by the GKSS-Research Center at the DORIS storage ring (HASYLAB at DESY, Hamburg, Germany; Beckmann *et al.* 2004, 2008) using a monochromatic beam of 14 keV. The wiggler source was set to a gap of 40 mm. The photon flux density during the experiment at the beamline BW2 is estimated to be about 2×10^{10} photons $\mathrm{mm}^{-2}\,\mathrm{s}^{-1}$). In order to enlarge the field of view, the experiment was performed with an asymmetric rotation axis position, shifted by 2 mm from the centre of the detection unit as used previously (e.g. Müller *et al.* (2007)). Using a detector with a field of view of $4.57 \times 3.05\ \mathrm{mm}^2$, 1440 projections were recorded during the rotation of the specimen by 360°. The pixel size amounted to 3.0 μm. The spatial resolution of the entire absorption-contrast set-up was

determined by 10 per cent of the modulation transfer function (MTF) (Müller *et al.* 2002*b*) corresponding to 6.48 μm. The twofold binning of the projected highly X-ray absorbing edge led to a reduced spatial resolution of 8.77 μm again determined by 10 per cent of the MTF.

2.4. Data processing

In order to improve the density resolution of the absorption-contrast dataset, the projections were binned twofold (Thurner *et al.* 2004). This consequently led to a pixel size of 6.0 μm comparable to the 5.1 μm pixel size of the phase-contrast data. The absorption-contrast tomograms were obtained by means of the standard filtered back-projection reconstruction algorithm (Kak & Slaney 2001). The phase-contrast projection dataset was reconstructed using a modified filter kernel (Hilbert transform) in combination with standard filtered back-projection algorithm (Faris & Byer 1988; Pfeiffer *et al.* 2007*b*,*c*). Grating interferometric tomography provides, along with the decrement of the real part of the refractive index, the absorption-contrast tomograms at the selected photon energy, i.e. the imaginary part of the refractive index. For the reconstruction of these absorption-contrast projections, the same standard filtered back-projection reconstruction algorithm as for the BW2 data was used.

As it is important to compare identical volumes, the datasets obtained from the different facilities were registered using a three-dimensional rigid algorithm (Andronache *et al.* 2008; Fierz *et al.* 2008) with six degrees of freedom, namely three translation and three rotation degrees. For the registration, the more precise values of the pixel sizes, namely (5.95 ± 0.02) μm for the absorption contrast and (5.06 ± 0.02) μm for the phase-contrast results had to be used. These values correspond to averaged pixel sizes that were determined by the defined moving of a narrow object over several thousand pixels. Because of the different nature of image modalities, the registration was performed using the classical maximization of mutual information (MI) principle (Viola & Wells 1995; Maes *et al.* 1996). For robust registration, the absorption-contrast dataset had to be filtered using a 5×5 pixel median filter. This filtered dataset was only used for the registration. As a result of the registration and the determination of the common volume, we obtained three equally oriented sets of three-dimensional data of the cerebellum termed 'absorption contrast BW2', 'absorption contrast ID19' and 'phase contrast ID19'.

For the analysis of the datasets, the histograms were approximated with a multi-Gaussian fit (Müller *et al.* 2002*a*) using the Levenberg–Marquardt algorithm in OriginPro 7.5 (OriginLab Corporation, Northampton, USA). The centre positions of the Gaussians on the abscissa then correspond to the absorption or decrement of the real part of the refractive index, and, for homogeneous objects, their width, expressed in terms of standard deviation, to the statistical errors of these values. For inhomogeneous objects, the standard deviation is basically dependent on the variation of the μ- or δ-values inside the different components.

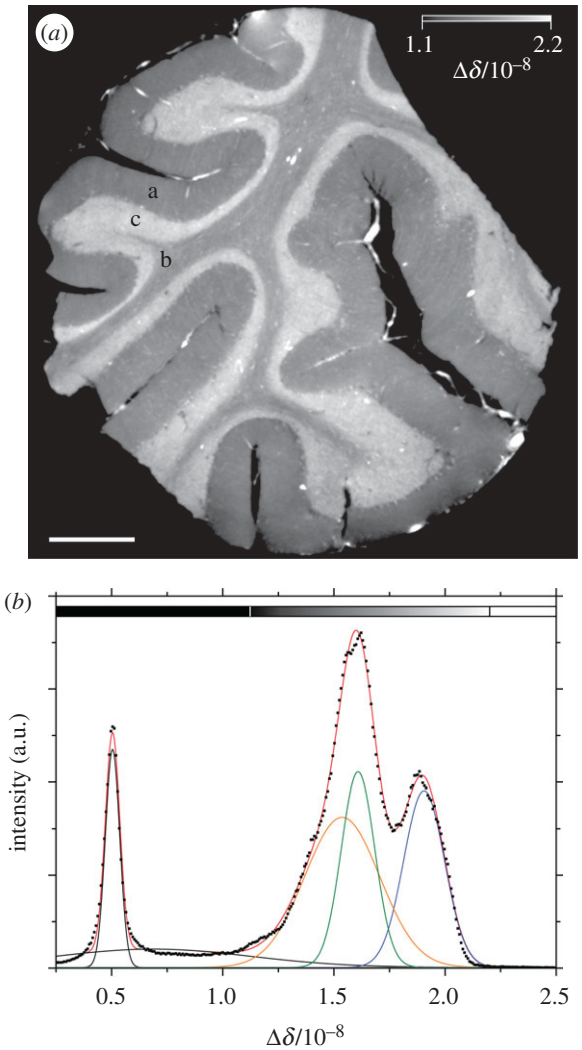

Figure 2. One reconstructed slice plus the appropriate histogram of the phase-contrast results showing three different strata and several blood vessels (bright regions in the slices that exceed the grey-scale range) of the human cerebellum. The mean value of the blood vessels amounts $\Delta\delta = 3.6 \times 10^{-8}$. The formalin peak (left peak in the diagram) has the value $\Delta\delta = 5.03 \times 10^{-9}$ with the standard deviation $\sigma_{\mathrm{form}} = 0.32 \times 10^{-9}$. Thus, the grey-scale range corresponds to 34 standard deviations of the formalin peak. The standard deviation is a measure of the homogeneity of the tissue or solution: the narrower the width the Gaussian is, the more homogeneous the substance. (*a*) Scale bar, 1 mm. (*b*) Orange line, stratum moleculare (a); green line, white matter (b); navy blue line, stratum granulosum (c).

3. RESULTS

3.1. Phase-contrast SRμCT

The reconstructed slice of the grating-based SRμCT measurement (figure 2*a*) allows clear differentiation between the four morphological features, i.e. stratum moleculare, stratum granulosum and white matter, as well as blood vessels. The value $\Delta\delta = \delta_{H_2O} - \delta$ describes the decrement of the real part of the refractive index relative to water δ_{H_2O}. The related histogram (figure 2*b*) shows besides the formalin peak at $\Delta\delta = 0.5 \times 10^{-8}$, two clearly distinguishable peaks with maxima at $\Delta\delta = 1.6 \times 10^{-8}$ and $\Delta\delta = 1.9 \times 10^{-8}$.

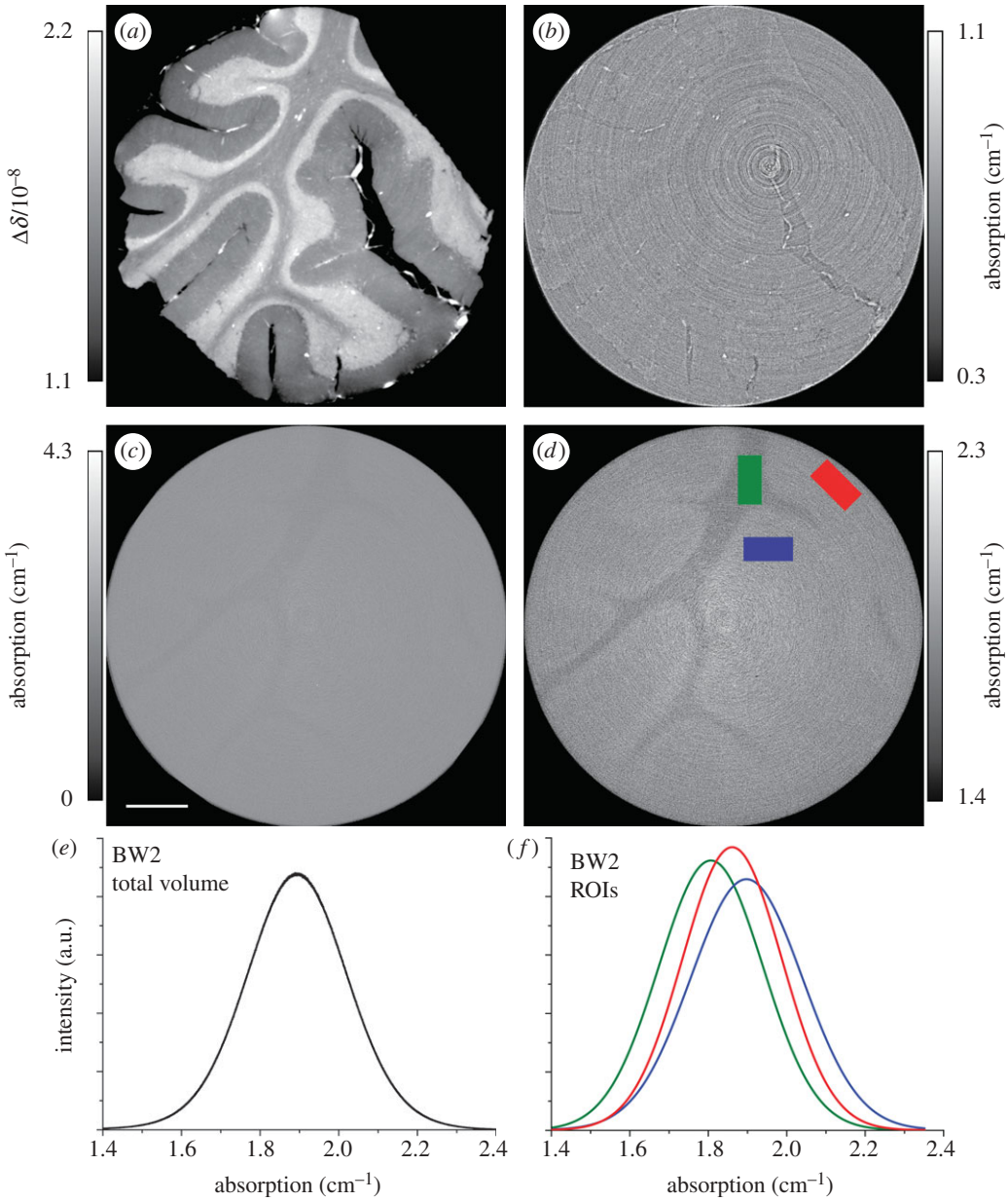

Figure 3. Grating interferometry phase-contrast reconstruction with a grey-scale range corresponding to 34 standard deviations of the formalin peak (*a*) compared with accordant BW2 absorption-contrast reconstruction with a grey-scale range corresponding to 34 (*c*) and 3 (*d*) standard deviations of the formalin peak. Figure (*b*) shows the absorption-contrast reconstruction obtained from grating interferometry with a grey-scale range of 3 standard deviations. Figure (*e*) demonstrates the histogram of the whole three-dimensional dataset whereas figure (*f*) illustrates the histogram of the areas labelled in figure (*d*), summed over 50 slices. ROI, region of interest.

Using a function composed of five Gaussians the histogram is reasonably well fitted, as shown by the solid red line in figure 2. The fit shows that the Gaussians corresponding to stratum moleculare and the white matter overlap so that a purely intensity-based segmentation is impossible. Fortunately, the stratum granulosum separates the two features and hence allows for segmentation of stratum moleculare and white matter.

The grey-scale range of the reconstructed slice corresponds to 34 standard deviations of the formalin peak $\sigma_{\mathrm{form}} \approx \mathrm{FWHM}_{\mathrm{form}}/2.35 = 3.2 \times 10^{-10}$. As it can be assumed that the distilled water has no significant density fluctuations, the standard deviation of the background signal in the reconstructed slice can be interpreted as the measurement resolution of the real part of the refractive index. Using the value of $\sigma_{\mathrm{H_2O}} = 2.3 \times 10^{-10}$ in equation (2.3), the corresponding electron density resolution is 0.15 electrons per nm^3 and the mass density sensitivity for aqueous specimens is 0.25 mg cm^{-3}. The standard deviation of water in the processed projections of $\sigma_{\mathrm{H_2O}} = 1.7 \times 10^{-8}$ rad can then be interpreted as the measurement sensitivity of the deflection angles.

The Gaussian fit (figure 2*b*) was also used to quantify the values of the decrement of the real part of the refractive index for the features inside the human cerebellum plus formalin. Here the values $\Delta\delta_{\mathrm{form}} = (0.50 \pm 0.03) \times 10^{-8}$ for the formalin, $\Delta\delta_{\mathrm{med}} = (1.61 \pm 0.08) \times 10^{-8}$ for the white matter, corresponding to the green-coloured Gaussian, $\Delta\delta_{\mathrm{mol}} = (1.54 \pm 0.17) \times 10^{-8}$ for the stratum

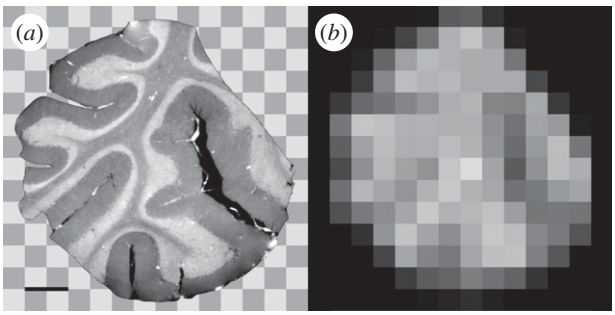

Figure 4. A 100-fold binning of the phase-contrast results reveals the distinction of the spatial resolution between SRμCT and contemporary medical MRT. For that, we assumed a pixel size of 0.5 mm for nowadays common medical high-resolution MR-results. The black bar corresponds to 1 mm.

moleculare (orange Gaussian) and $\Delta\delta_{\text{gran}} = (1.90 \pm 0.09) \times 10^{-8}$ for the stratum granulosum (blue Gaussian) were obtained.

3.2. Density resolution in absorption and phase-contrast SRμCT

As it is impossible to calculate the precise absorption values of the three different substances, formalin and white and grey matter, by plotting Gaussian fits in the histogram of the whole dataset (figure 3*e*), volumes representing the corresponding substances were chosen as represented in figure 3*d*. The dimension of the selected blocks was 65 × 135 × 50 voxels. Using Gaussian plots, we obtained the values $\mu_{\text{form}} = (1.86 \pm 0.13)\ \text{cm}^{-1}$ for the formalin, $\mu_{\text{med}} = (1.79 \pm 0.14)\ \text{cm}^{-1}$ for the white matter and $\mu_{\text{grey}} = (1.90 \pm 0.14)\ \text{cm}^{-1}$ for grey matter (figure 3*f*). Thus, the measurement sensitivity of the 'absorption contrast BW2' results in a value of $0.13\ \text{cm}^{-1}$.

3.3. Spatial resolution of SRμCT

The internal stresses in formalin fixed bone were shown to be in the range of 50–70 MPa (Almer & Stock 2007). In order to quantify the shrinkage of the human brain during formalin fixation, the whole brain was additionally scanned on a Verio 3 Tesla whole body MRT scanner (Siemens HealthCare, Erlangen, Germany) with 0.7 mm isotropic pixel size before the extraction of the explored cerebellum block and compared with scans at different steps of fixation. The preliminary results show that the volume shrinkage of the whole human brain during 10 per cent formalin fixation is around 8 per cent.

Because of the huge differences in the pixel sizes, it was impossible to rigidly register the MRT results with the grating interferometry volume (figure 4*a*) in order to find the exact position and orientation of the small block inside the brain. To demonstrate the huge discrepancy of the pixel sizes between the clinical MRT- and SRμCT-results and resultant failure of the registration, a 100-fold binning of the grating-based phase-contrast results was performed (figure 4*b*). The resulting pixel size of 0.5 mm matches the current typical medical high-resolution data.

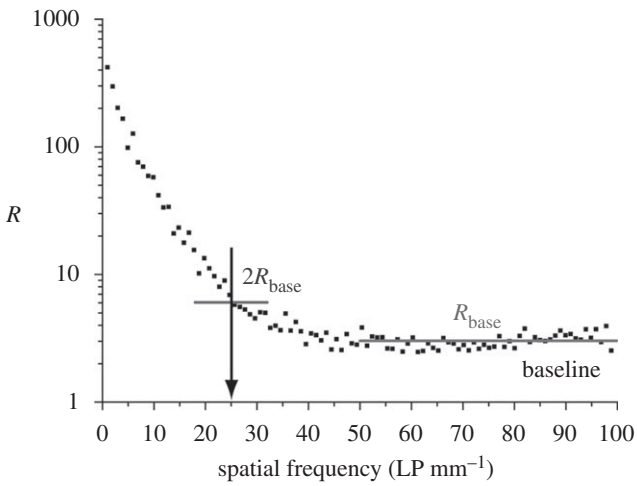

Figure 5. For the calculation of the spatial resolution, the ratio between $\text{rSP}_{\text{struc}}$ of a tomogram ROI with a fine structure and rSP_{back} of a tomogram ROI with background (water) was plotted over spatial frequency.

The lowest limit of the spatial resolution achievable with a grating X-ray interferometer (Weitkamp *et al.* 2005) is given by twice the absorption grating period p_2. In general, it becomes worse for higher Talbot orders. Resolution can be further limited by the detection system. An estimation of the spatial resolution of the experimental data was obtained by means of Fourier analysis of the processed projections and reconstructed tomograms. For that purpose, the *radial spectral power* (rSP) of a fine structure containing slice region of interest (200 × 200 pixels) was calculated ($\text{rSP}_{\text{struc}}$) and divided by the rSP of a background region of the same size (rSP_{back}) (Modregger *et al.* 2007). This ratio R was plotted against the spatial frequency in figure 5. The baseline observed for frequencies higher than 50 line pairs per millimetre (LP mm^{-1}) was associated with noise. Finally, the spatial resolution was estimated as the first observed frequency greater than twice the mean value of the baseline R_{base}. This value (25 LP mm^{-1}) corresponds to a peak to peak distance of 40 μm. The spatial resolution was taken as half of this value, amounting to 20 μm as given for instance by Wang *et al.* (1991). Other calculations with different regions of interest of the tomograms resulted in an uncertainty of only 1 μm. The same procedure was followed to determine the spatial resolution of the processed projections. The estimation resulted in a better spatial resolution of the projections compared with the tomograms, amounting to (16.5 ± 0.5) μm. This value indicates the spatial resolution averaged over the two dimensions of the projection. The larger value of the reconstructed slices arises from the blurring during the application of the reconstruction algorithm.

3.4. Three-dimensional visualization of the grating-based phase-contrast results

The representation in the upper part of figure 6 is a virtual cut through a three-dimensional rendering of the phase-contrast tomogram. Using an intensity-based

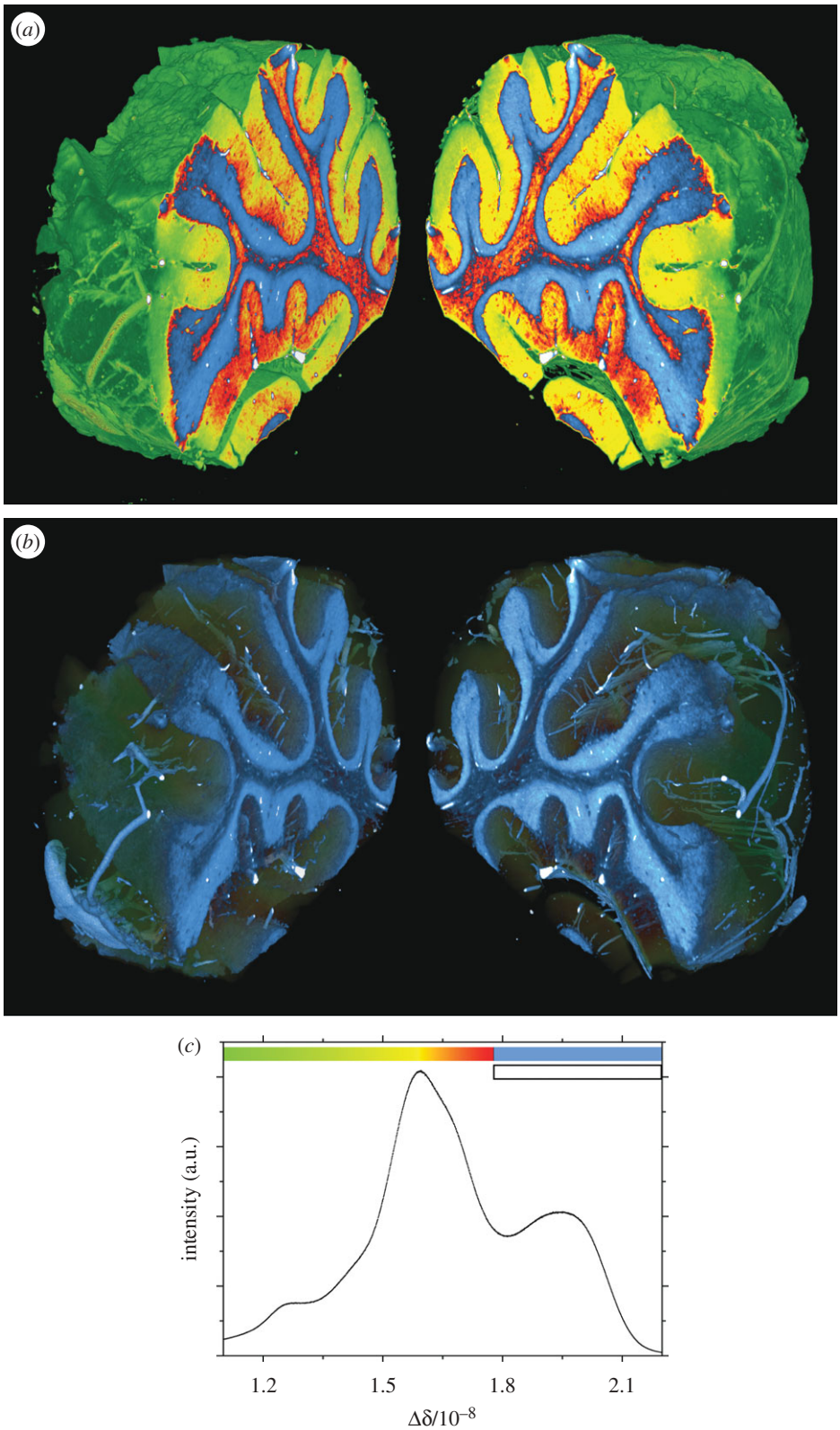

Figure 6. The phase-contrast three-dimensional rendering of the whole specimen with a virtual cut through it (*a*,*b*) demonstrates the feasibility to segment one of the shown structures by simple intensity-based segmentation. For the segmentation of the stratum granulosum the quantitative threshold values correspond to the grey-scale values of figure 2*a*. These values are also shown in the histogram of the whole dataset (*c*).

labelling of the dataset one can differentiate between the stratum granulosum (blue), the stratum moleculare (green–yellow–red gradient) and the white matter (mainly red). For the labelling, the threshold values of the histogram of the tomogram shown in figure 2 were applied. The intensity-based segmentation of the stratum granulosum as represented in the middle of figure 6 was generated increasing the transparency of voxels with $\Delta\delta$-values in the green–yellow–red gradient labelled range. This choice of the segmentation

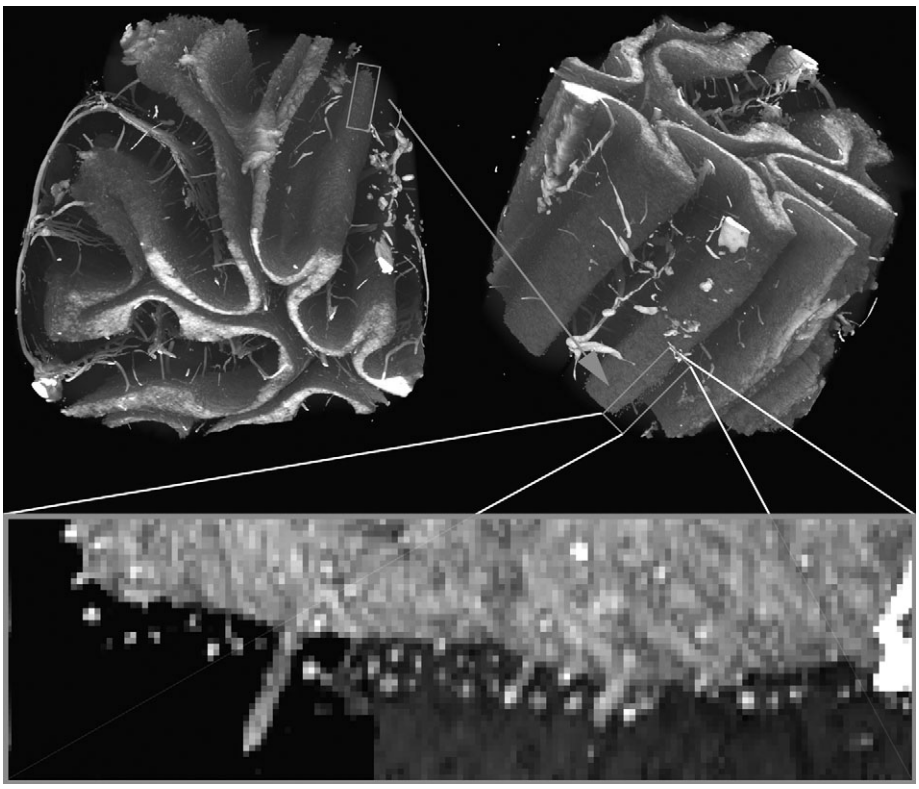

Figure 7. Another phase-contrast three-dimensional rendering of the specimen presumably shows the so-called Purkinje cells. The grey-scale values correspond to the white bar in the histogram in figure 6*c*.

highlights the characteristic course of blood vessels inside the cerebellum with an entrance angle of 90° to the surface of the stratum granulosum. The characteristics of the blood vessels can be seen even better in figure 7. The grey-scale range of this representation corresponds to the $\Delta\delta$-values illustrated by the white bar in the histogram of figure 6. Besides the blood vessels, one can detect spherical microstructures with diameters of around 40 μm, 7–10 pixels wide, along the surface of stratum granulosum. On the basis of the location and the size of these features they are identified as the Purkinje cells.

4. DISCUSSION

Examining the histogram of one reconstructed slice (figure 2*b*), one observes that only four of the five Gaussians can be clearly related to known morphological structures of the human cerebellum. The fifth Gaussian with the largest half width describes the $\Delta\delta$-values lying between the formalin and stratum moleculare related peaks. Therefore, this Gaussian basically corresponds to the partial volume between these two components. Aside from the partial volume one finds an additional peak at $\Delta\delta = 1.3 \times 10^{-8}$, which appears rather as a shoulder. This shoulder becomes more obvious in the histogram of the entire three-dimensional dataset (figure 6*c*). The quantitative analysis of the shoulder reveals that the related $\Delta\delta$-values are located in areas of the cerebellum that were in direct contact with the formalin solution during the whole fixation period. Obviously, the formalin treatment of the human cerebellum changes the electron density at the tissue periphery.

The usefulness of the absorption-contrast data of the second-generation synchrotron radiation source is restricted because intensity-based segmentation is in fact fairly complicated. The histogram of figure 3*f* illustrates the crucial overlap of the absorption values of the three components. Note that the formalin solution yields absorption values just between those of white and grey matter. Hence, another solution with higher or lower absorption should be applied. Phosphate buffer, for example, leads to higher absorption values (Germann *et al.* 2008) and is, therefore, better suited. The intensity-based segmentation of white and grey matter, however, remains difficult, since the green-coloured and blue-coloured peaks overlap in a significant manner.

The detailed comparison between the absorption-contrast data obtained from grating interferometry (figure 3*b*) and the conventional ones (figure 3*d*), both grey-scaled to three times the standard deviations σ_{form} of the formalin peak, shows that the grating interferometry results yield less contrast between the internal features. This behaviour is expected because the selected photon energy is too high for optimal image acquisition. The optimal energy of 14 keV for aqueous specimen with diameter $D = 1$ cm can be calculated from the equation $\mu = 2/D$ (Grodzins 1983*a*,*b*). The sharp features present in the ID19 absorption data concern internal interfaces as the results of edge enhancement and are not seen in the optimized absorption-contrast tomogram from the second-generation source.

The measurement sensitivity for the real part of the refractive index of the presented phase-contrast measurement (perhaps better termed as the resolution power) is enormously high and corresponds to an angular resolution of 1.7×10^{-8} rad. This corresponds to the size a small lorry parked on the Moon would appear from Earth. This value, however, is a factor of three lower than that found in a previous study (Pfeiffer *et al.* 2009). The difference is predominantly due to data binning, which resulted in 15 μm voxel size compared with the 5 μm in the present study (Thurner *et al.* 2004). Further influencing parameters are the operation mode of the insertion device, the photon energy that was around 10 per cent lower in the present study, the modified exposure time and the higher resolving FReLoN unit.

Comparing the histograms of a single phase-contrast slice (figure 2*b*) with the entire dataset (figure 6*c*), one recognizes significant differences. The slice-wise cross-check of the histograms allows us to conclude that the broader peaks in figure 6 are the consequence of relatively small displacements of the peak positions from slice to slice. It leads to rather higher uncertainties of the $\Delta\delta$-values given in §3.1.

The sensitivity of the grating interferometry, however, is so high that individual Purkinje cells become visible without the application of any contrast agent. This is the most important result of the study, and to the best of our knowledge the first time that X-ray tomography permitted the identification of unstained cells in human soft tissue. So far, only osmium-stained ganglion cells have been made visible in absorption-contrast mode (Lareida *et al.* 2009).

The three-dimensional images of the Purkinje cells can be weighted against histological results. First, the grating-based SRμCT data only show the larger features, namely the perikaryon and not the detailed dendritic tree, which propagates outwards in the direction of the stratum moleculare. Besides the limited spatial resolution, the reason behind this could be similar electron density values of the dendritic tree and the stratum moleculare. Second, according to the present tomographic study, the maximum diameter of an individual Purkinje cell corresponds to about 40 μm and the cell area to around 700 μm^2. There is no doubt that the visualization of the Purkinje cells is close to the limit of the experimental set-up. A true measurement of the cell size is therefore impossible. Nevertheless, the spatial resolution of 20 μm, together with the pixel size of 5.1 μm, allows a rough estimate of the diameters of the features detected, which correspond in location and size to the Purkinje cells often visualized in two-dimensional histological slices shown, for instance, in Fatemi *et al.* (2002). Our results agree well with the data of Fatemi *et al.*, who obtained for the cell area (661 ± 85) μm^2 from unfixed cerebellar sections but less with the result of stained histological slices by Tran *et al.* (1998), who found (374 ± 34) μm^2. The alcohol fixation process apparently induces a significant shrinkage of the cells. Third, the two-dimensional Purkinje cell density of normal brain was determined at (16 ± 4) cells per mm^2 (Jeste *et al.* 1984), a value also obtained from our tomographic data. Note, the density of Purkinje cells is reduced by diseases such as schizophrenia, autism, Huntington's disease and other movement disorders (Jeste *et al.* 1984; Tran *et al.* 1998; Fatemi *et al.* 2002). In summary, there remains no doubt that the micro-features shown in figure 7 are the Purkinje cells, since the location, size, shape and density are very well comparable with the histological results.

5. SUMMARY AND CONCLUSION

Grating-based X-ray tomography offers superior three-dimensional images of the human cerebellum, which not only allow for the discrimination between grey and white matter but also between stratum moleculare and stratum granulosum. Additionally, the clear visualization of non-stained individual Purkinje cells is possible—a technique that is unrivalled so far.

The authors gratefully acknowledge M. Müller-Gerbl and P. Zimmermann for the organization and extraction of the human brain, A. Morel and M. Imholz for the brain specimen blocking and A. Andronache for availability of the rigid registration tool. The project was partially funded by Swiss National Science Foundation (CR23I2_125 406) and was supported by the ESRF (proposal MD-407) and HASYLAB, DESY (proposal II-20060035 EC) by allocation of beam time. F. Pfeiffer acknowledges support of the DFG cluster of Excellence Munich-Centre for Advanced Phototonics.

REFERENCES

Almer, J. D. & Stock, S. R. 2007 Micromechanical response of mineral and collagen phases in bone. *J. Struct. Biol.* **157**, 365–370. (doi:10.1016/j.jsb.2006.09.001)

Andronache, A., von Siebenthal, M., Székely, G. & Cattin, P. 2008 Non-rigid registration of multi-modal images using both mutual information and cross-correlation. *Med. Image Anal.* **12**, 3–15. (doi:10.1016/j.media.2007.06.005)

Beckmann, F., Bonse, U., Busch, F., Günnewig, O. & Biermann, T. 1995 A novel system for X-ray phase-contrast microtomography. *Hasylab Annu. Rep.* **2**, 691–692.

Beckmann, F., Donath, T., Dose, T., Lippmann, T., Martins, R. V., Metge, J. & Schreyer, A. 2004 Microtomography using synchrotron radiation at DESY: current status and future developments. *Proc. SPIE* **5535**, 1–10. (doi:10.1117/12.560561)

Beckmann, F., Herzen, J., Haibel, A., Müller, B. & Schreyer, A. 2008 High density resolution in synchrotron-radiation-based attenuation-contrast microtomography. *Proc. SPIE* **70781D**, 1–13. (doi:10.1117/12.794617)

Bonse, U. & Hart, M. 1965 An X-ray interferometer. *Appl. Phys. Lett.* **6**, 155–156. (doi:10.1063/1.1754212)

Brooks, R. A., Di Chiro, G. & Keller, M. R. 1980 Explanation of cerebral white–gray contrast in computed tomography. *J. Comput. Assist. Tomogr.* **4**, 489–491. (doi:10.1097/00004728-198008000-00016)

Chapman, D. *et al.* 1997 Diffraction enhanced X-ray imaging. *Phys. Med. Biol.* **42**, 2015–2025. (doi:10.1088/0031-9155/42/11/001)

Cloetens, P., Barrett, R., Baruchel, J., Guigay, J.-P. & Schlenker, M. 1996 Phase objects in synchrotron radiation hard X-ray imaging. *J. Phys. D Appl. Phys.* **29**, 133–146. (doi:10.1088/0022-3727/29/1/023)

Cloetens, P., Ludwig, W., Baruchel, J., Van Dyck, D., Van Landuyt, J., Guigay, J. P. & Schlenker, M. 1999 Holotomography: quantitative phase tomography with micrometer resolution using hard synchrotron radiation X-rays. *Appl. Phys. Lett.* **75**, 2912–2914. (doi:10.1063/1.125225)

David, C., Nöhammer, B., Solak, H. H. & Ziegler, E. 2002 Differential X-ray phase contrast imaging using a shearing interferometer. *Appl. Phys. Lett.* **81**, 3287–3289. (doi:10.1063/1.1516611)

David, C., Bruder, J., Rohbeck, T., Grünzweig, C., Kottler, C., Diaz, A., Bunk, O. & Pfeiffer, F. 2007 Fabrication of diffraction gratings for hard X-ray phase contrast imaging. *Microelectron. Eng.* **84**, 1172–1177. (doi:10.1016/j.mee.2007.01.151)

Davis, T. J., Gao, D., Gureyev, T. E., Stevenson, A. W. & Wilkins, S. W. 1995 Phase-contrast imaging of weakly absorbing materials using hard X-rays. *Nature* **373**, 595–598. (doi:10.1038/373595a0)

Dilmanian, F. A., Zhong, Z., Ren, B., Wu, X. Y., Chapman, L. D., Orion, I. & Thomlinson, W. C. 2000 Computed tomography of X-ray index of refraction using the diffraction enhanced imaging method. *Phys. Med. Biol.* **45**, 933–946. (doi:10.1088/0031-9155/45/4/309)

Faris, G. W. & Byer, R. L. 1988 Three-dimensional beam-deflection optical tomography of a supersonic jet. *Appl. Opt.* **27**, 5202–5212. (doi:10.1364/AO.27.005202)

Fatemi, S. H., Halt, A. R., Realmuto, G., Earle, J., Kist, D. A., Thuras, P. & Merz, A. 2002 Purkinje cell size is reduced in cerebellum of patients with autism. *Cell. Mol. Neurobiol.* **22**, 171–175. (doi:10.1023/A:1019861721160)

Fierz, F. C. *et al.* 2008 The morphology of anisotropic 3D-printed hydroxyapatite scaffolds. *Biomaterials* **29**, 3799–3806. (doi:10.1016/j.biomaterials.2008.06.012)

Fitzgerald, R. 2000 Phase-sensitive X-ray imaging. *Phys. Today* **53**, 23–26. (doi:10.1063/1.1292471)

Förster, E., Goetz, K. & Zaumseil, P. 1980 Double crystal diffractometry for the characterization of targets for laser fusion experiments. *Krist. Tech.* **15**, 937–945. (doi:10.1002/crat.19800150812)

Germann, M., Morel, A., Beckmann, F., Andronache, A., Jeanmonod, D. & Müller, B. 2008 Strain fields in histological slices of brain tissue determined by synchrotron radiation-based micro computed tomography. *J. Neurosci. Methods* **170**, 149–155. (doi:10.1016/j.jneumeth.2008.01.011)

Grodzins, L. 1983*a* Optimum energies for X-ray transmission tomography of small samples. *Nucl. Instrum. Methods* **206**, 541–545. (doi:10.1016/0167-5087(83)90393-9)

Grodzins, L. 1983*b* Critical absorption tomography of small samples. *Nucl. Instrum. Methods* **206**, 547–552. (doi:10.1016/0167-5087(83)90394-0)

Jeste, D. V., Barban, L. & Parisi, J. 1984 Reduced purkinje cell density in Huntington's disease. *Exp. Neurol.* **85**, 78–86. (doi:10.1016/0014-4886(84)90162-6)

Kak, A. C. & Slaney, M. 2001 *Principles of computerized tomographic imaging* Philadelphia, PA: SIAM.

Lareida, A., Beckmann, F., Schrott-Fischer, A., Glueckert, R., Freysinger, W. & Müller, B. 2009 High-resolution X-ray tomography of the human inner ear: synchrotron radiation-based study of nerve fiber bundles, membranes, and ganglion cells. *J. Microsc.* **234**, 95–102. (doi:10.1111/j.1365-2818.2009.03143.x)

Maes, F., Collignon, A., Vandermeulen, D., Marchal, G. & Suetens, P. 1996 Multi-modality image registration by maximization of mutual information. In *Proc. IEEE Math. Meth. in Biomed. Im. Anal., 21–22 June 1996, San Francisco, CA*, pp. 14–22. San Francisco, CA: Society for Industrial and Applied Mathematics. (doi:10.1109/MMBIA.1996.534053)

Maksimenko, A., Ando, M., Hiroshi, S. & Yuasa, T. 2005 Computed tomographic reconstruction based on X-ray refraction contrast. *Appl. Phys. Lett.* **86**, 124105. (doi:10.1063/1.1891305)

Modregger, P., Lübbert, D., Schäfer, P. & Köhler, R. 2007 Spatial resolution in Bragg-magnified X-ray images as determined by Fourier analysis. *Phys. Status Solidi a* **204**, 2746–2752. (doi:10.1002/pssa.200675685)

Momose, A. 2005 Recent advances in X-ray phase imaging. *Jpn J. Appl. Phys. Part 1* **44**, 6355–6367. (doi:10.1143/JJAP.44.6355)

Momose, A. & Fukuda, J. 1995 Phase-contrast radiographs of nonstained rat cerebellar specimen. *Med. Phys.* **22**, 375–379. (doi:10.1118/1.597472)

Momose, A., Kawamoto, S., Koyama, I., Hamaishi, Y., Takai, K. & Suzuki, Y. 2003 Demonstration of X-ray Talbot interferometry. *Jpn. J. Appl. Phys., Part 2* **42**, 866–868.

Momose, A., Yashiro, W., Takeda, Y., Suzuki, Y. & Hattori, T. 2006 Phase tomography by X-ray Talbot interferometry for biological imaging. *Jpn J. Appl. Phys. Part 1* **45**, 5254–5262. (doi:10.1143/JJAP.45.5254)

Müller, B., Beckmann, F., Huser, M., Maspero, F. A., Székely, G., Ruffieux, K., Thurner, P. J. & Wintermantel, E. 2002*a* Non-destructive three-dimensional evaluation of a polymer sponge by micro-tomography using synchrotron radiation. *Biomol. Eng.* **19**, 73–78. (doi:10.1016/S1389-0344(02)00014-X)

Müller, B. *et al.* 2002*b* Non-destructive three-dimensional evaluation of biocompatible materials by microtomography using synchrotron radiation. *Proc. SPIE* **4503**, 178–188. (doi:10.1117/12.452843)

Müller, B. *et al.* 2007 Morphology of bony tissues and implants uncovered by high-resolution tomographic imaging. *Int. J. Mater. Res.* **98**, 613–621.

Pfeiffer, F., Bunk, O., David, C., Bech, M., Le Duc, G., Bravin, A. & Cloetens, P. 2007*a* High-resolution brain tumor visualization using three-dimensional X-ray phase contrast tomography. *Phys. Med. Biol.* **52**, 6923–6930. (doi:10.1088/0031-9155/52/23/010)

Pfeiffer, F., Bunk, O., Kottler, C. & David, C. 2007*b* Tomographic reconstruction of three-dimensional objects from hard X-ray differential phase contrast projection images. *Nucl. Instrum. Methods Phys. Res. Sect. A* **580**, 925–928. (doi:10.1016/j.nima.2007.06.104)

Pfeiffer, F., Kottler, C., Bunk, O. & David, C. 2007*c* Hard X-ray phase tomography with low-brilliance sources. *Phys. Rev. Lett.* **98**, (doi:10.1103/PhysRevLett.98.108105)

Pfeiffer, F., David, C., Bunk, O., Poitry-Yamate, C., Grütter, R., Müller, B. & Weitkamp, T. 2009 High-sensitivity phase-contrast tomography of rat brain in phosphate buffered saline. *J. Phys. Conf. Ser.* **186**, 0120461. (doi:10.1088/1742-6596/186/1/012046)

Pradel, A., Langer, M., Maisey, J. G., Geffard-Kuriyama, D., Cloetens, P., Janvier, P. & Tafforeau, P. 2009 Skull and brain of a 300-million-year-old chimaeroid fish revealed by synchrotron holotomography. *Proc. Natl Acad. Sci. USA* **106**, 5224–5228. (doi:10.1073/pnas.0807047106)

Reznikova, E., Mohr, J., Boerner, M., Nazmov, V. & Jakobs, J. 2008 Soft X-ray lithography of high aspect ratio SU8 submicron structures. *Microsyst. Technol.* **14**, 1683–1688. (doi:10.1007/s00542-007-0507-x)

Snigirev, A. A., Snigireva, I., Kohn, V., Kuznetsov, S. & Schelokov, I. 1995 On the possibilities of X-ray phase contrast microimaging by coherent high-energy synchrotron radiation. *Rev. Sci. Instrum.* **66**, 5486–5492. (doi:10.1063/1.1146073)

Thurner, P. J., Beckmann, F. & Müller, B. 2004 An optimization procedure for spatial and density resolution in hard X-ray micro-computed tomography. *Nucl. Instrum. Methods Phys. Res. B* **225**, 599–603. (doi:10.1016/j.nimb.2004.05.027)

Tran, K. D., Smutzer, G. S., Doty, R. L. & Arnold, S. E. 1998 Reduced Purkinje cell size in the cerebellar vermis of elderly patients with schizophrenia. *Am. J. Psych.* **155**, 1288–1290.

Trepel, M. 2008 *Neuroanatomie/Struktur und Funktion* Munich, Germany: Urban & Fischer.

Viola, P. & Wells, W. M. 1995 Alignment by maximization of mutual information. In *Proc. 5th Int. Conf. on Comp. Vis., 20–23 June, Cambridge, MA*, pp. 16–23. (doi:10.1109/ICCV.1995.466930)

Wang, L., Ho, P. P., Liu, C., Zhang, G. & Alfano, R. R. 1991 Ballistic 2-D imaging through scattering walls using an ultrafast optical Kerr gate. *Science* **253**, 769–771. (doi:10.1126/science.253.5021.769)

Weitkamp, T., Diaz, A., David, C., Pfeiffer, F., Stampanoni, M., Cloetens, P. & Ziegler, E. 2005 X-ray phase imaging with a grating interferometer. *Opt. Expr.* **13**, 6296–6304. (doi:10.1364/OPEX.13.006296)

Weitkamp, T., David, C., Kottler, C., Bunk, O. & Pfeiffer, F. 2006 Tomography with grating interferometers at low-brilliance sources. *Proc. SPIE* **6318**, 63180S. (doi:10.1117/12.683851)

Weitkamp, T., David, C., Bunk, O., Bruder, J., Cloetens, P. & Pfeiffer, F. 2008 X-ray phase radiography and tomography of soft tissue using grating interferometry. *Eur. J. Radiol.* **68S**, S13–S17.

Weitkamp, T. *et al.* 2010 Status and evolution of the ESRF beamline ID19. *AIP Conf. Proc.* **1221**, 33–38. (doi:10.1063/1.3399253)